

<https://doi.org/10.1038/s43246-024-00564-7>

Nitric oxide-generating metallic wires for enhanced metal implants



Federico Mazur¹, Yingzhu Zhou¹, Gervase Ng^{1,2}, Qingqing Fan¹, Andy-Hoai Pham¹, Cyrille Boyer^{1,2} & Rona Chandrawati¹

Metallic implants are integral in modern medicine, offering excellent biocompatibility and mechanical properties. However, implant-related infections pose a major challenge. Current drug delivery methods, such as surface-coated and drug-eluting implants, are limited by finite drug supplies and complex manufacturing steps. Recent approaches like local drug synthesis, including enzyme-prodrug therapies, present innovative solutions but are hampered by the inherent limitations of enzymes as well as complex procedures. Here, we introduce a simpler alternative: using the intrinsic properties of implant materials to activate prodrugs. Through a simple thermal treatment, metallic implants gain catalytic properties to locally generate nitric oxide, an antibacterial agent. Our findings show this treatment is non-toxic to cells, does not affect cell proliferation rates, and effectively inhibits bacterial biofilm formation. This material-driven approach eliminates the need for external chemical or enzymatic interventions, offering a promising solution to prevent implant-related infections and improve patient outcomes in implant medicine.

Metallic implant materials have gained significant clinical importance in the medical field, with the global orthopaedic market being expected to grow from USD\$45.19 billion in 2023 to \$64.27 billion by 2030¹. The rapid growth in biomaterial development has led to an increase in metal-based medical products including dental implants, craniofacial plates and screws, clips, valves, catheters, and bone fixation devices, among various others². Although ceramics, polymers, metals, and their alloys, can be used as implant materials, the majority are metal-based, most commonly titanium, stainless steel, or cobalt-based alloys³. Metal-based implants are preferred over other materials due to their excellent biocompatibility, favourable mechanical properties, good corrosion resistance, low cost, and stability^{4,5}. However, implant-associated infections are considered one of the most common complications, ranging from 0.5 to up to 30% of cases, depending on the type of orthopaedic surgery^{6–10}. This is because the implants themselves are susceptible to the formation of a biofilm on their surface, which protects bacteria from the patient's immune system and are usually resistant to antibiotics¹¹. These infections are a serious issue as they can lead to implant failure, longer treatments, the need for more antibiotics, surgical interventions, as well as a significant economic burden on the patient¹². A promising approach to tackle this problem involves the use of localized therapeutic strategies¹³.

Two main approaches can be taken to achieve localized therapy. The first involves using drug-eluting implants which slowly release the agent around the microenvironment of the implant with efficient biological

utilization rate. Research into these systems is plentiful, with conventional implants including anti-inflammatory drugs¹⁴, antibiotics¹⁵, growth factors¹⁶, and various others¹⁷. However, this approach is limited by a finite drug reservoir, which restricts the longevity of the drug delivery. The second approach involves localized synthesis of a drug through the conversion of a prodrug into an active agent. Materials can be engineered to decompose natural prodrugs present in the body, enabling continuous generation of the therapeutic agent. For instance, a well-known approach involves enzyme-prodrug therapies that rely on enzyme-containing coatings for prodrug bioconversion, such as for the synthesis of anti-proliferative drugs¹⁸, gasotransmitters¹⁹, or antibacterials²⁰. A key challenge in enzyme-activated prodrug therapy is the biodegradability and membrane-impermeable nature of exogenous enzymes. This requires the use of suitable carriers to effectively protect and deliver them. Finding carriers that can efficiently navigate these biological barriers while maintaining the stability and activity of the enzymes is a significant hurdle²¹. Furthermore, despite the inherent selectivity of enzymes, ensuring that the prodrug activation occurs exclusively at the target site, without affecting other tissues, is difficult. The body's complex environment and the presence of similar enzymes or substrates in non-target tissues can affect the specificity of these therapies. Therefore, challenges also lie in harnessing the enzymes' selectivity in a way that maximizes therapeutic efficacy while minimizing off-target effects²². Considering these limitations, an alternative more attractive approach involves the use of inherent qualities present in the implant material itself to convert

¹School of Chemical Engineering and Australian Centre for Nanomedicine (ACN), The University of New South Wales, Sydney, 2052 NSW, Australia. ²Cluster for Advanced Macromolecular Design (CAMD), The University of New South Wales, Sydney, 2052 NSW, Australia. e-mail: rona.chandrawati@unsw.edu.au

the prodrug. This was recently serendipitously demonstrated in Zelikin's research group, where iron-containing metallic implants were shown to mediate the hydrolysis of glucuronide prodrugs to antibiotics, inhibiting bacterial growth around the material²³. Metal/metal ion-catalysed nitric oxide (NO) generation from prodrugs has garnered significant interest in biomedical applications due to its well-known antibacterial, antibiofilm, and wound healing therapeutic potential²⁴. As such, various studies have investigated the ability of numerous transition metal ions (e.g. Cu²⁺, Co²⁺, Fe²⁺)^{25,26} as well as metal-based complexes²⁷ towards NO prodrug decomposition. Despite the extensive research in this area, there remains a need for approaches that can enhance the efficiency and practicality of NO generation for real-world biomedical applications.

The present study was conceived after an opportune observation where thermally treated wires, henceforth referred to as calcinated wires, could catalytically degrade S-nitrosothiols, which are NO-releasing prodrugs. This discovery opened up a new avenue for material engineering, specifically in the context of localized drug synthesis, where a simple calcination process can endow metallic implant materials with therapeutic properties. Herein, we evaluate the ability of calcinated stainless steel, stellite, titanium, and silver wires to catalytically generate NO from an endogenous NO prodrug, S-nitrosoglutathione (GSNO). GSNO was chosen as the NO prodrug as it is one of the most biologically abundant NO donors^{28,29}. Specifically, we have determined the effect that calcination has on NO generation by evaluating variables including wire length, GSNO concentration, alternative NO prodrugs, calcination conditions, and recyclability. Furthermore, the cytotoxicity, effect on the rate of cell proliferation, and biofilm inhibition properties of the calcinated wires were also assessed. Collectively, we present a simple calcination method to modify commonly used metallic implant materials with potential therapeutic benefits via endogenous NO generation without requiring chemicals or enzymatic catalysis.

Results and discussion

Effect of wire length on NO generation

Stainless steel, stellite, titanium, and silver wires were calcinated and screened for their capacity to generate NO when exposed to an NO donor, specifically GSNO. Briefly, non-calcinated or calcinated wires for each

material were placed in glass vials, followed by the addition of 200 μ L of 50 μ M GSNO in PBS, and incubated at 37 $^{\circ}$ C for 24 h. After incubation, a Griess assay was performed on the supernatant to quantify the NO generated (Fig. 1). This procedure was carried out using 0, 5, 10, 15, or 20 wires (5 mm length, 0.25 mm diameter), where an increasing number of wires correspond to a greater wire length. The choice to increase the number of wires rather than the wire length facilitates practical lab-scale procedures. To illustrate, it is more practical to use 20 wires that are 5 mm in length rather than 1 wire that is 100 mm in length. However, the exposed surface area is greater compared to the latter single-wire approach. Nevertheless, the difference in surface area, even with 20 wires, is less than 2.4%, which can be considered negligible. This extra surface area was calculated assuming the wires are perfect cylinders. As an example, the surface area of 1 wire 100 mm in length is 78.64 mm². On the other hand, the surface area of 20 wires 5 mm in length is 80.5 mm² (4.03 mm² \times 20 wires) which accounts for a 2.37% increase when using our "length" approach. The percentage increase difference is lower when using fewer wires.

As shown in Fig. 1, when comparing calcinated wires with their non-calcinated counterpart, a difference in NO generation was only observed for stainless steel and stellite wires, while little-to-no difference was observed when using titanium or silver wires. For stainless steel, a linear increase in NO generation with an increasing number of both non-calcinated or calcinated wires can be observed. This means that non-calcinated stainless steel wires have inherent catalytic properties to decompose GSNO and generate NO, however the calcination process further improves the catalytic activity. The inherent catalytic activity of non-calcinated wires will be discussed later. Stellite demonstrated a greater efficiency in generating NO from GSNO compared to stainless steel. This is because only 5 wires were required to reach the NO generation plateau within the same time frame. Nevertheless, as with stainless steel, a linear increase in NO generation was observed for an increasing number of non-calcinated wires. This catalytic activity inherent in stainless steel and stellite wires can be attributed to the presence of transition metal elements (Fe, Ni, Mn, Cr, Co) within these alloys. Transition metals are known to act as effective catalysts due to their capacity to either donate or accept electrons from a reagent, depending on the nature of the reaction. Studies have shown that multimetallic catalysts abundant in

Fig. 1 | NO generation from increasing amounts of non-calcinated or calcinated metal wires. Cumulative NO generation after incubating 0, 5, 10, 15, or 20 non-calcinated or calcinated **a** stainless steel, **b** stellite, **c** titanium, or **d** silver wires in 200 μ L of 50 μ M GSNO in PBS for 24 hours at 37 $^{\circ}$ C. * p < 0.05, ** p < 0.01, *** p < 0.001 (ANOVA followed by Tukey post-hoc test). $n \geq 3$; error bars represent standard deviation.

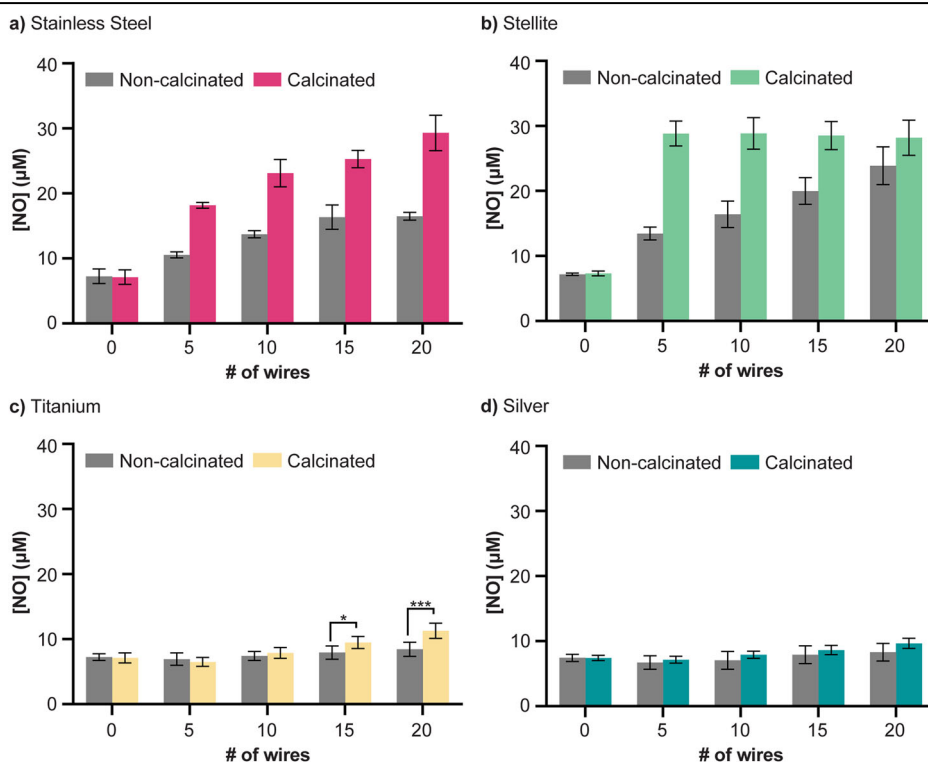
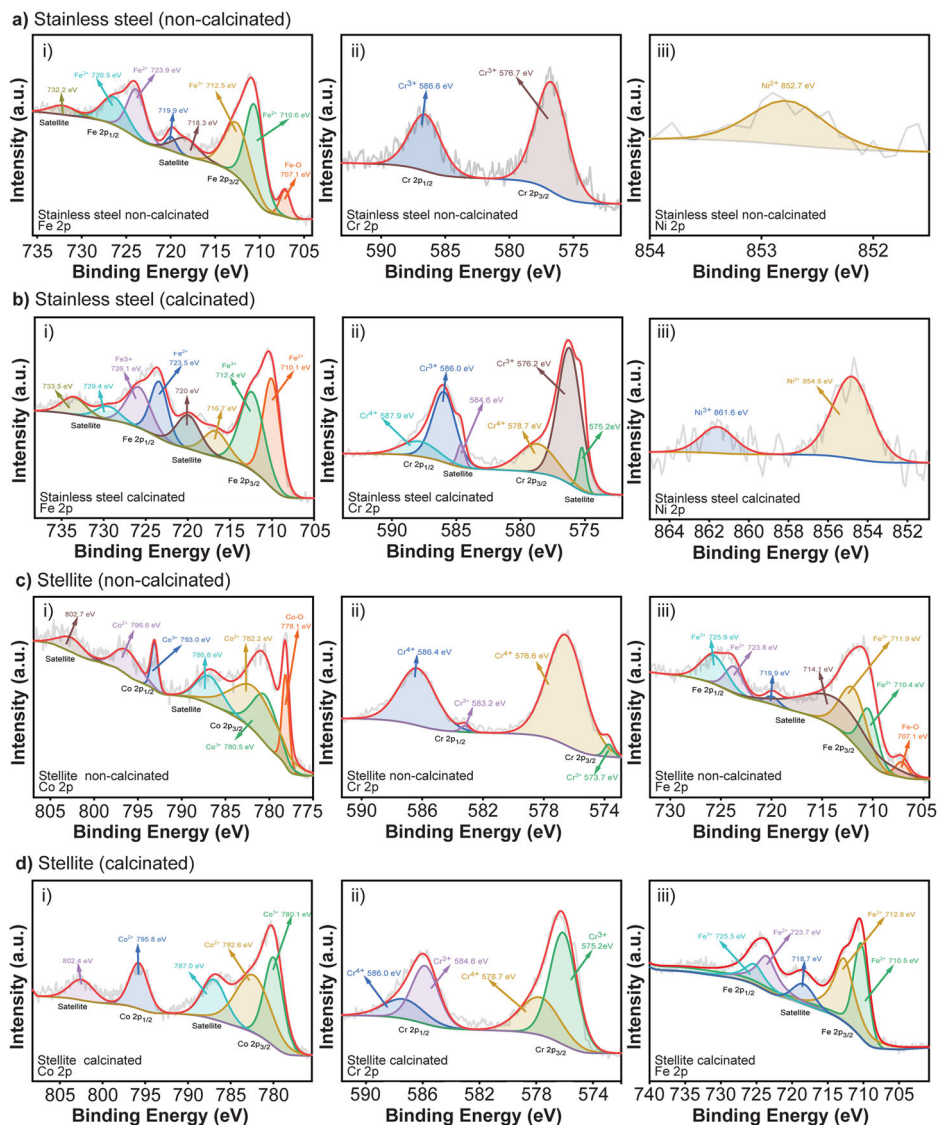


Fig. 2 | XPS spectra of the three most abundant elements before and after calcination of stainless steel and stellite wires. XPS spectra for a non-calcinated and b calcinated stainless steel wires. i) Fe 2p, ii) Cr 2p, iii) Ni 2p. XPS spectra for c non-calcinated and d calcinated stellite wires. i) Co 2p, ii) Cr 2p, iii) Fe 2p.



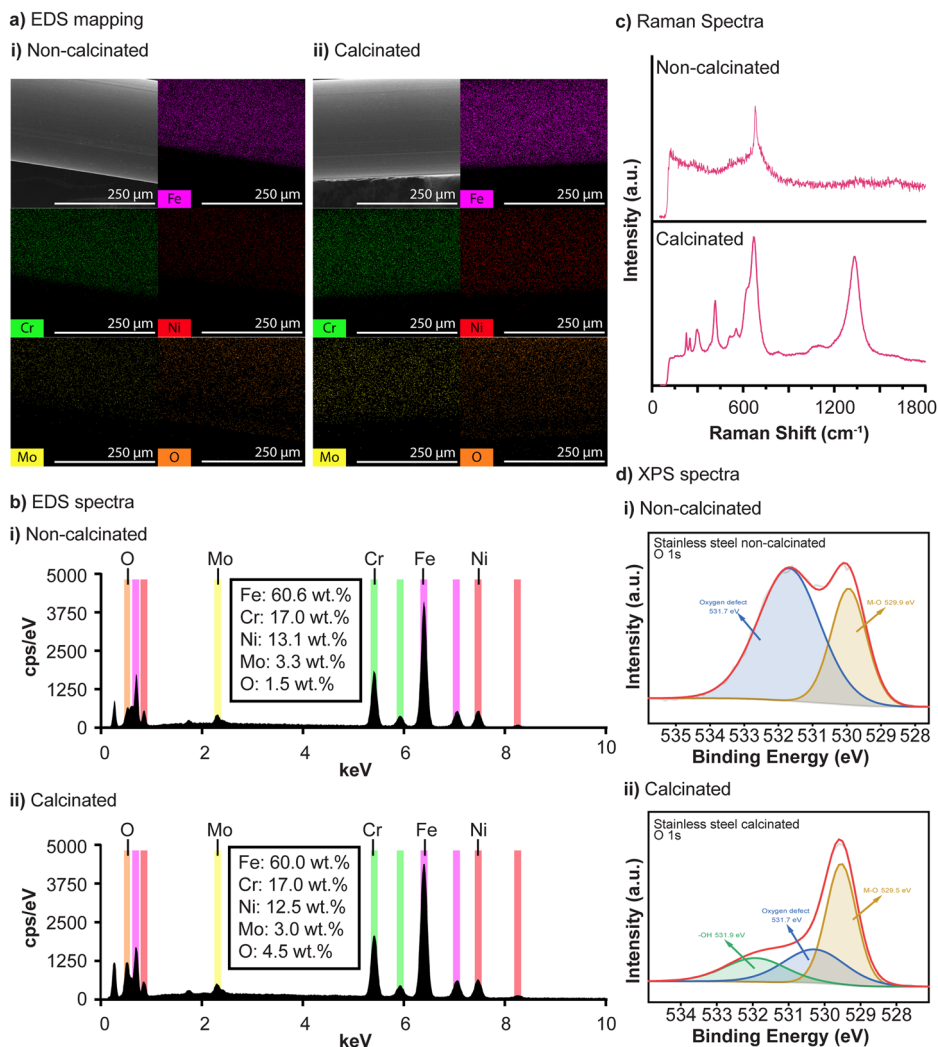
these metal elements exhibit catalytic properties^{30,31}. Thus, materials like stainless steel and stellite have a great potential to exhibit such properties. However, they are commonly used after being surface modified (e.g. acid leaching or coatings³²), as has been shown in the fields of pollutant abatement³³, organic synthesis³⁴, and clean energy³⁵. This is because they exhibit insufficient active sites for catalytic reactions and require significant energy (high overpotential) to initiate the reaction^{36,37}, with many cases showing no activity unless surface modified³⁸. These results show that GSNO can be catalytically degraded by unmodified stainless steel or stellite wires, whilst calcination further improves this degradation. To the best of our knowledge, this is the first reported case documenting this finding.

To investigate the contributing factors of this enhanced catalytic activity, we performed X-ray Photoelectron Spectroscopy (XPS). The spectra obtained for both materials before and after calcination showed the presence of the respective transition metal elements, but after calcination the high-resolution spectra show a greater coexistence of different oxidation states for all species (Fig. 2 for most abundant elements, Supplementary Figs. 1, 2 for all others, Supplementary Table 1 for binding energies of each species for both materials). The ability of transition metals to adopt various oxidations has also been associated with enhanced catalytic activity³⁹. In other words, their ability to easily change oxidation states allows them to act as electron transfer catalysts in many reactions.

Furthermore, it has been shown that treatment via calcination or surface etching of these metals can activate their surface, endowing greater catalytic properties⁴⁰. High-temperature conditions can cause these components to migrate from the bulk phase to the surface of the material, generating an oxide layer that significantly alters their physicochemical properties. To confirm the formation of this oxide layer after calcination, Energy-Dispersive X-ray Spectroscopy (EDS), Raman Spectroscopy, and XPS were carried out. For the former, an increase in the relative weight percentage of oxygen from 1.5 to 4.5% for stainless steel (Fig. 3a, b) and 1.2 to 5.1% for stellite (Fig. 4a, b) was observed. The Raman spectra were also shown to significantly change for both materials after calcination, indicating the presence of the oxide layer (Figs. 3c, 4c), as previously demonstrated^{41,42}. Finally, for XPS, an increase in the ratio between M-O and oxygen defects is indicative of the presence of more metal oxides on the surface of the materials (Figs. 3d, 4d).

Moreover, this oxide layer formation can also lead to an increase in the surface roughness and thereby exposure of the active metal species^{43–45}. To quantify differences in surface roughness, atomic force microscopy (AFM) was carried out and showed that the calcination process increased the root-mean-square roughness (Rq) of stainless steel and stellite wires by 2.6 and 19.7 times, respectively (Figs. 5, 6). In addition to the difference in metal alloy composition, this large difference in surface roughness can explain the higher catalytic activity of

Fig. 3 | EDS elemental mapping and spectra as well as Raman and XPS (O 1s) spectra before and after calcination of stainless steel wires. EDS a) elemental mapping and b) spectra of i) non-calcinated and ii) calcinated stainless steel wires. c) Raman spectra of stainless steel wires before and after calcination. d) XPS spectra (O 1s) of i) non-calcinated and ii) calcinated stainless steel wires.



stellite compared to stainless steel. It should be noted that titanium wires also exhibited a change in Raman spectra upon calcination (Supplementary Fig. 3), indicative of the formation of an oxide layer⁴⁶, however a negligible change in surface roughness was observed (Supplementary Fig. 4). This could explain the trend observed in Fig. 1 which depicts statistically significant NO generation, albeit small, when using >15 wires. On the other hand, silver wires did not show any significant changes in Raman spectra (Supplementary Fig. 5) when compared to the other three materials, as well as a negligible change in surface roughness (Supplementary Fig. 6). Since titanium and silver did not generate NO, they are not considered viable materials and will not be investigated further. Considering that both surface roughness and surface elements were altered following the heat treatment process, it was essential to determine which change had a more significant impact on NO generation. To investigate this, the surface roughness of stainless steel and stellite wires was modified using chemical etching (HCl) or mechanical abrasion (sandpaper, 120-grit), and an increase in surface roughness was observed (Supplementary Figs. 7, 8). Notably, neither surface roughness treatment affected NO generation in stainless steel wires compared to calcination, indicating that surface elements play a more critical role in NO generation. Conversely, mechanically abraded stellite wires generated NO to a similar extent as calcinated wires, suggesting that surface roughness is a significant factor for stellite (Supplementary Fig. 9). Although chemical etching led to a small increase in NO generation compared to untreated samples, it was not as effective as mechanical abrasion. Further optimization of treatment variables for chemical

etching could potentially enhance NO generation. Nevertheless, calcination remains the ideal treatment to simply and consistently lead to NO generation for both materials and will be utilized henceforth.

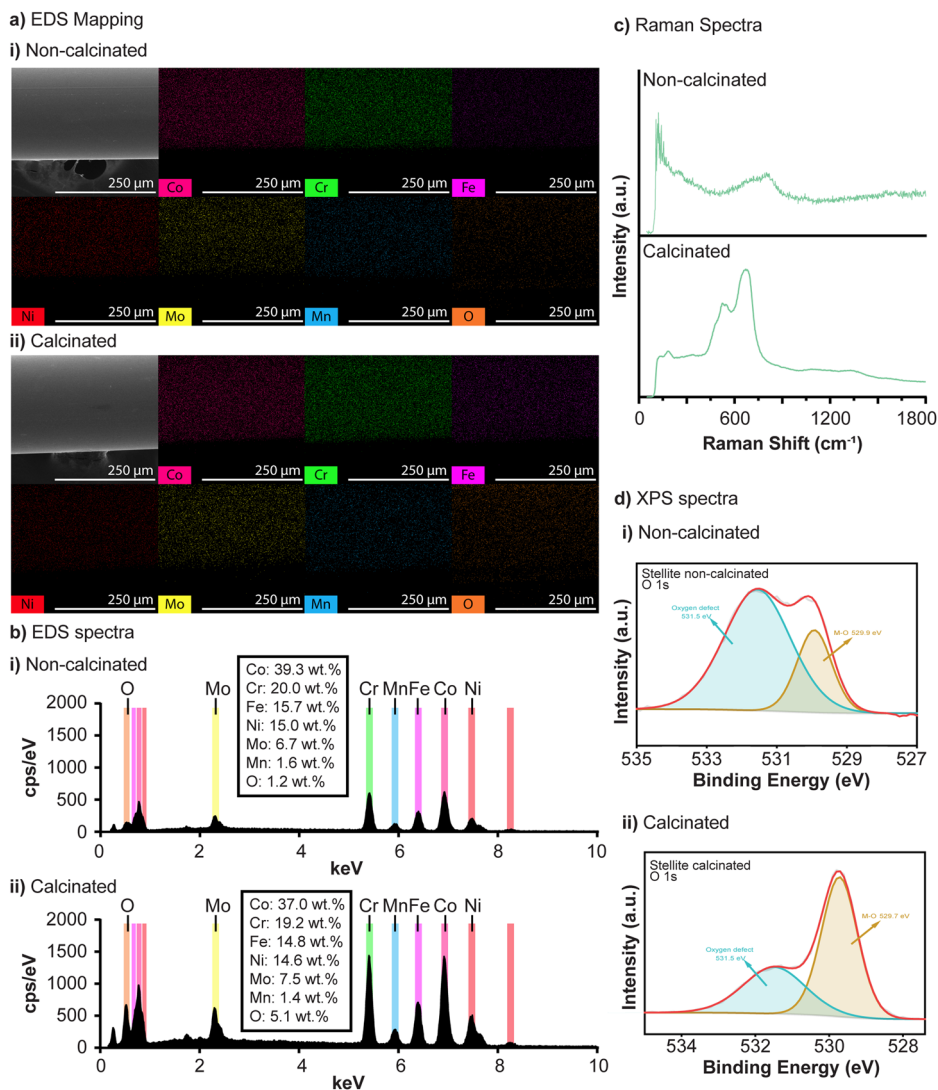
Kinetic NO generation

Upon confirming only stainless steel and stellite wires could generate NO from GSNO, their generation profile was determined. Understanding the NO generation kinetics of the material is crucial in evaluating its effectiveness. Maintaining a constant generation of NO over time is preferred over a burst generation when considering antibacterial applications. While the latter case may initially eliminate bacteria, there is a potential risk of bacterial regrowth later. Therefore, it is essential to assess whether the generation rate of the wires exhibits a burst or constant NO generation over time. To obtain this profile, a Griess assay was performed at various time points on the supernatant of 5 non-calcinated or calcinated wires that had been incubated for 24 h at 37 °C with 200 μL of 50 μM GSNO in PBS. A linear profile was observed for both cases, suggesting a stable generation profile can be achieved (Fig. 7a, b). Consistent with the previous section, stellite showed an averaged generation rate 57% higher compared to stainless steel for the same number of wires. These results in conjunction with the previous section highlight the tunability of NO generation via material choice and number (or length) of wires.

Effect of GSNO concentration on NO generation

In addition to evaluating the kinetic generation profile of both materials, the effect of GSNO concentration on NO generation was also investigated. This

Fig. 4 | EDS elemental mapping and spectra as well as Raman and XPS (O 1s) spectra before and after calcination of stellite wires. EDS **a** elemental mapping and **b** spectra of i) non-calcinated and ii) calcinated stellite wires. **c** Raman spectra of stellite wires before and after calcination. **d** XPS spectra (O 1s) of i) non-calcinated and ii) calcinated stellite wires.



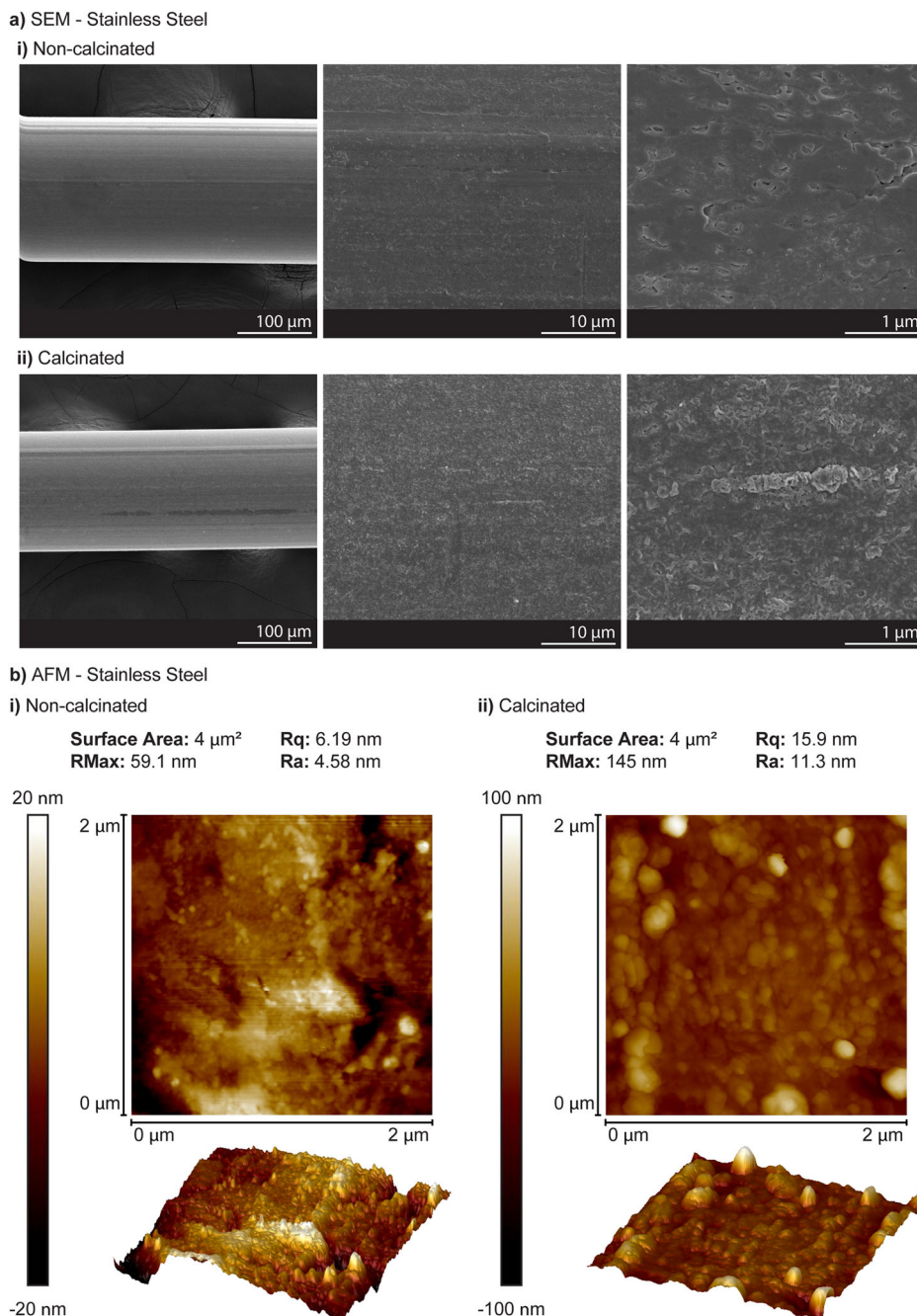
is because NO has concentration-dependent effects⁴⁷, therefore achieving tunable generation profiles that are biologically and therapeutically relevant is a desired feature. To achieve this, 5 non-calcinated or calcinated wires were incubated with 200 μ L of 0, 12.5, 25, 50, 100, or 200 μ M GSNO in PBS for 24 h at 37 $^{\circ}$ C. A Griess assay was carried out and, as expected for both stainless steel and stellite, NO generation increased with increasing GSNO concentration (Fig. 7c, d). The same trend was also observed for other systems which generate NO from GSNO using polymeric amines⁴⁸, ceria nanoparticles⁴⁹, zinc oxide particles⁵⁰, or metal-organic frameworks⁵¹. Therefore, in addition to material choice and number of wires, the GSNO concentration can also be used to tune NO generation.

Alternative donors for NO generation

Thus far, GSNO has been used as the NO donor as it is a natural NO prodrug present in the body and is therefore suitable to enable localized and sustained NO generation⁵². However, various other NO donors can be considered to expand potential applications for these heat-treated wires. Structural variations between NO donors can lead to significantly different NO-generation mechanisms. There are three main mechanisms by which NO can be generated from NO donors: (i) spontaneous generation through thermal or photochemical self-decomposition, (ii) enzymatic oxidation/hydrolysis through metabolic activation, or (iii) chemical reactions with acids, alkalis, metals, or thiols⁵³. GSNO falls within the latter mechanism. NO donors from each category were chosen and incubated with non-

calcinated and calcinated wires for both materials to determine whether NO could be generated. For the spontaneous generation donors, DPTA NONOate, DETA NONOate, and NOC-5 were chosen. β -gal NONOate was chosen as a donor of the enzymatic hydrolysis mechanism, while SNAP was included as an exogenous (rather than endogenous, as is the case with GSNO) donor, which generates NO via chemical reactions. Briefly, non-calcinated or calcinated wires were incubated with 200 μ L of 50 μ M DPTA NONOate, DETA NONOate, NOC-5, β -gal NONOate, SNAP, or GSNO (Fig. 7e, f). In contrast to previous sections, the incubation time was reduced from 24 to 0.5 h since the former was too long to show any difference between non-calcinated and calcinated wires. As expected, there was no difference in NO generation between non-calcinated or calcinated wires for NO donors which generate via the spontaneous mechanism. In other words, the spontaneous generation rate of these donors is more rapid than the benefit that could have been provided by the wires, if any. Similarly, the NO donor that relies on enzymatic hydrolysis, β -gal NONOate, did not show any difference in NO generation for either stainless steel or stellite wires. This is to be expected given that β -Gal-NONOate generates NO following activation by β -galactosidase⁵⁴. Nevertheless, β -gal NONOate was still evaluated to determine whether calcinated wires could potentially demonstrate enzyme-mimicking properties. Finally, SNAP was able to generate NO for both wire materials. Interestingly, stainless steel wires were able to generate more NO from SNAP compared to stellite wires, 41.3 vs. 27.8 μ M NO, respectively. This is in contrast to GSNO, where stellite wires proved to

Fig. 5 | FE-SEM and AFM before and after calcination of stainless steel wires. **a** FE-SEM images of i) non-calcinated and ii) calcinated stainless steel wires. **b** AFM images of i) non-calcinated and ii) calcinated stainless steel wires.



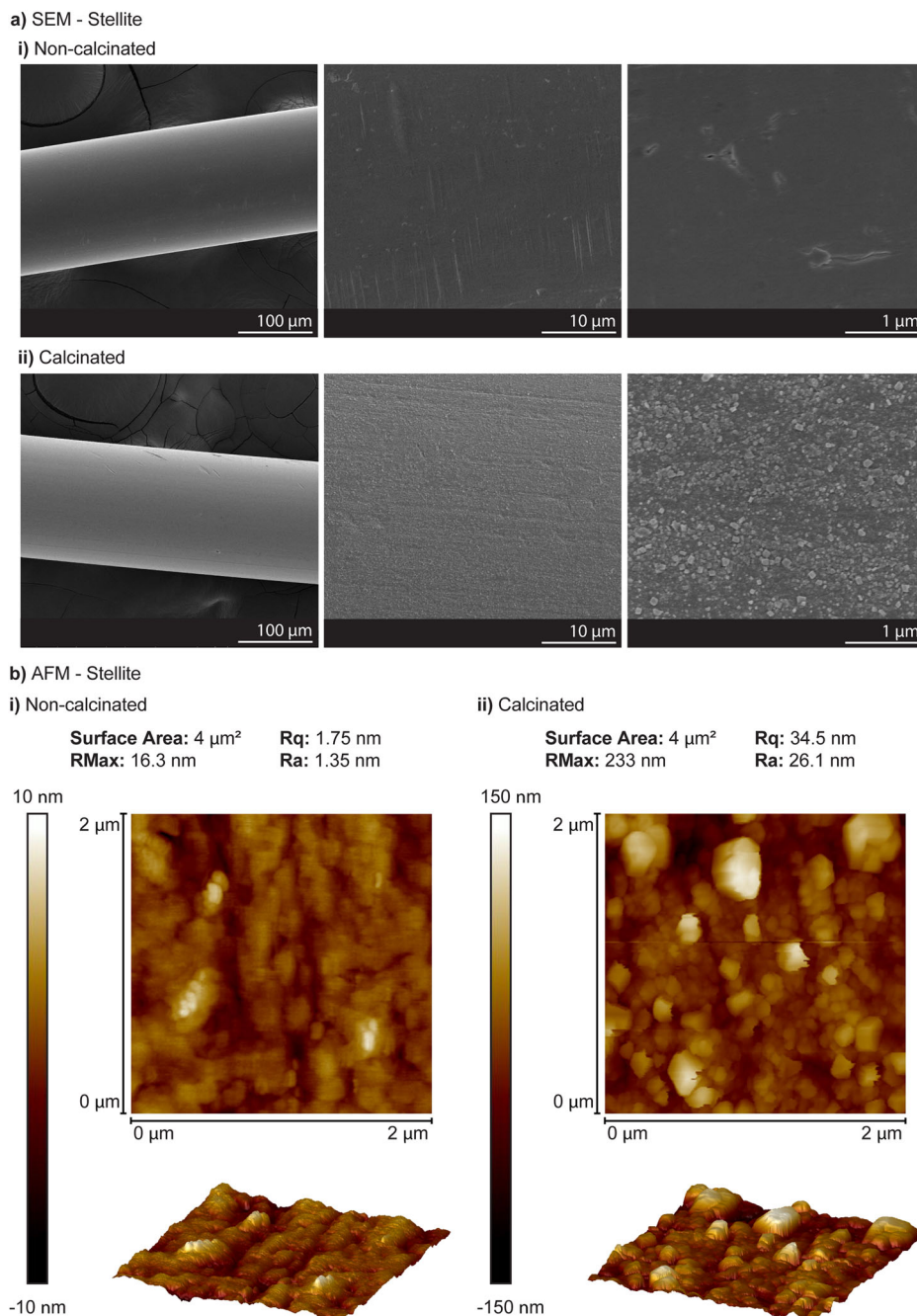
be more efficient than stainless steel (Fig. 1). Finally, despite both SNAP and GSNO falling under the same generation mechanism category, SNAP shows significantly greater NO generation rates compared to GSNO. To clarify, a greater amount of NO is generated over a shorter time period. This corresponds with the known stabilities of each compound, with SNAP being less stable than GSNO at these reaction conditions⁵⁵.

Effect of calcination conditions on NO generation

As previously discussed, heat treatment of both stainless steel and stellite wires can cause transition metal components within these alloys to migrate towards the surface, generating an oxide layer that alters their physico-chemical properties. Differences in calcination temperature and time can result in changes in the abundance of major elements in the oxide layer⁵⁶. Therefore, the effect of temperature and time were evaluated to determine whether differences in these variables could enhance the catalytic properties

of the wires. First, the effect of calcination temperature was investigated by heat treating stainless steel or stellite wires for 0.5 h at 300, 600, or 900 °C. Then, 5 non-calcinated and calcinated wires were incubated with 200 μL of 50 μM GSNO in PBS for 8 h (Fig. 8). It should be noted that 8 h incubation was used instead of 24 h to ensure the NO generation plateau was not reached and each condition could be compared. Notably, stainless steel showed negligible-to-no NO generation for both 300 and 900 °C. These results correspond with the Raman spectra obtained for each condition, where only 600 °C calcination led to a different spectrum corresponding to Fe_2O_3 (hematite)⁴¹, while the other temperatures are similar to the control, corresponding to Fe_3O_4 (magnetite)⁵⁷. On the other hand, stellite showed similar NO generation when using 600 and 900 °C calcination temperatures, while 300 °C resulted in no generation of NO. Interestingly, the Raman spectra peaks for both 300 and 600 °C are similar, corresponding to Cr_2O_3 and Co_3O_4 (first and second major peak, respectively)⁴². Since the spectra

Fig. 6 | FE-SEM and AFM before and after calcination of stellite wires. a FE-SEM images of i) non-calcinated and ii) calcinated stellite wires. **b** AFM images of i) non-calcinated and ii) calcinated stellite wires.



are similar, it suggests that a likely reason for the lack of NO generation could be due to the difference in the amount of oxide layer formed and surface roughness. On the other hand, the spectra for 900 °C also show the peaks corresponding to Cr_2O_3 and Co_3O_4 , with additional peaks around 300 and 1350 cm^{-1} . Since the difference in NO generation between 600 and 900 °C is negligible, a lower calcination temperature is preferable from an economic point of view. Therefore, these results show that the optimal calcination temperature for both stainless steel and stellite wires is 600 °C.

Having confirmed the optimal calcination temperature of 600 °C, the calcination time was then investigated. Briefly, the wires were calcinated for 0.5, 1, or 2 h, and evaluated for their NO generating capacity (Fig. 9). Similar trends can be observed for calcination times as were observed with calcination temperatures. Briefly, for stainless steel negligible NO generation was shown when calcinating for 0.5 and 2 h when compared to the non-calcinated counterpart, while calcinating for 1 h resulted in NO generation.

On the other hand, stellite showed similar NO generation when calcinating for 1 and 2 h while a 0.5 h calcination led to a reduction of approximately 50% in NO generation. Interestingly, the Raman spectra were similar for all cases, regardless of calcination time, suggesting that differences in NO generation arise from differences in the quantity of oxide layer formed and surface roughness.

Recyclability of wires

A crucial aspect to consider when evaluating long-term sustained delivery is the ability to generate NO even after multiple uses. As such, this variable was examined for both stainless steel and stellite wires. As before, 5 non-calcinated or calcinated wires were incubated with 200 μL of 50 μM GSNO in PBS for 24 h at 37 °C, followed by a Griess assay on the supernatant to quantify the cumulative NO generated. The wires were then washed by dipping with ultrapure water and the process was repeated a total of 5 times

Fig. 7 | NO release from non-calcinated and calcinated stainless steel and stellite wires. Cumulative NO generation after incubating 5 non-calcinated or calcinated **a** stainless steel or **b** stellite wires in 200 μL of 50 μM GSNO in PBS over a 24 h time period at 37 $^{\circ}\text{C}$. Cumulative NO generation after incubating 5 non-calcinated or calcinated **c** stainless steel or **d** stellite wires in 200 μL of 0, 12.5, 25, 50, 100, or 200 μM GSNO in PBS over a 24 h time period at 37 $^{\circ}\text{C}$. Cumulative NO generation after incubating 5 non-calcinated or calcinated **e** stainless steel or **f** stellite wires in 200 μL of 50 μM DPTA NONOate, DETA NONOate, NOC-5, β -gal NONOate, or SNAP in PBS over a 0.5 h time period at 37 $^{\circ}\text{C}$. $n \geq 3$; error bars represent standard deviation.

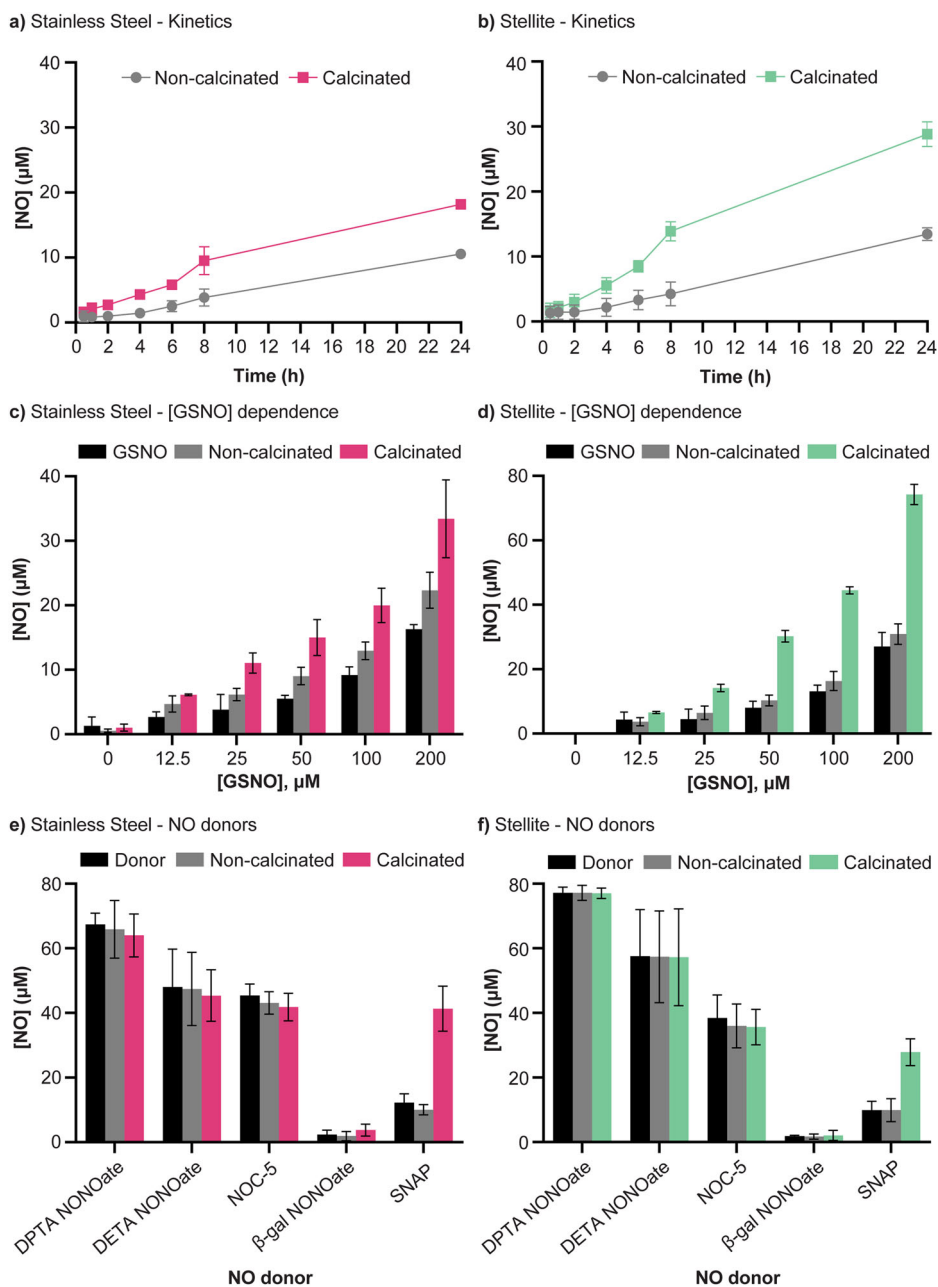


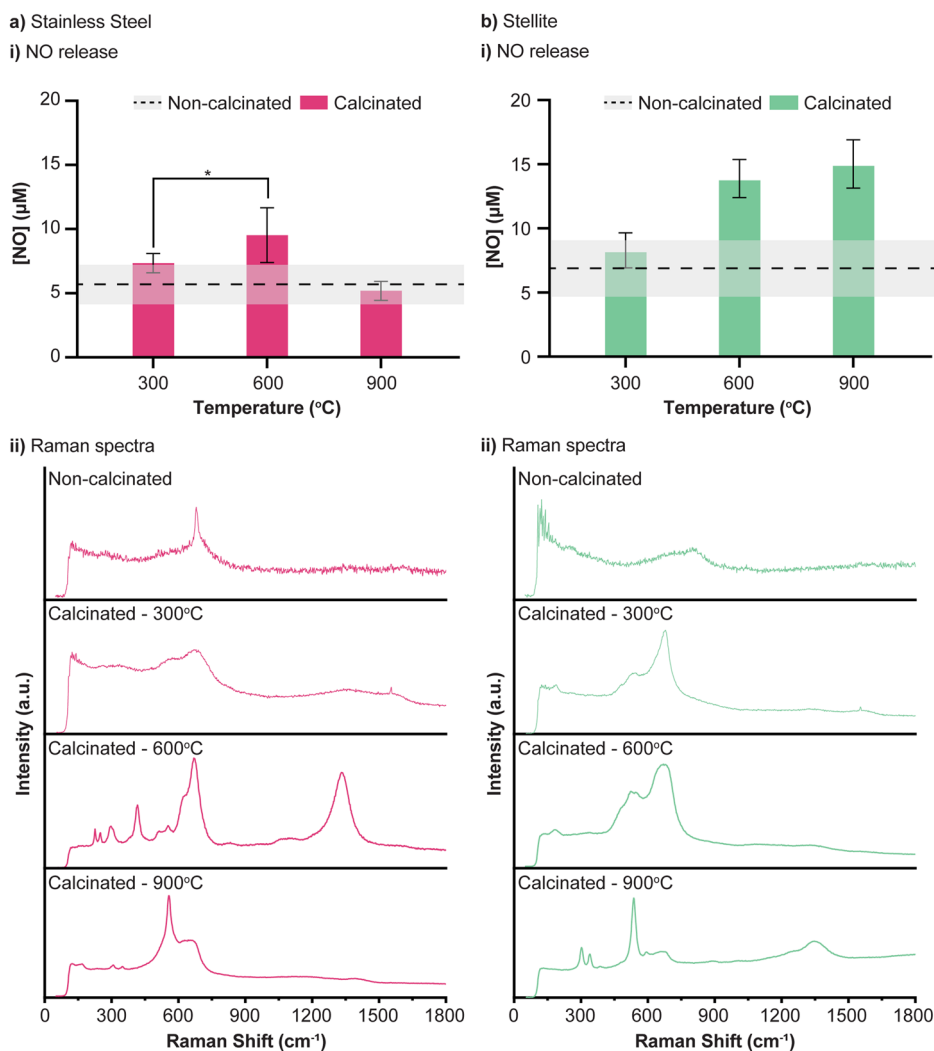
(Fig. 10a, b). Interestingly, stainless steel showed a significant decrease in NO generation of approximately 64% after 1 use, with no NO being generated after 2 uses. On the other hand, stellite wires showed no decrease in NO generation even after 5 uses, suggesting greater stability over multiple uses. These results indicate that stellite is a more attractive material for sustained NO generation. Additionally, calcinated stainless steel and stellite wires were stored for 10 months in a glass vial at room temperature to evaluate the effect of long-term storage. A small decrease in NO generation was observed for stainless steel, while no decrease was observed for stellite wires (Fig. 10c). It is also worth noting the wire samples after GSNO incubation showed negligible-to-small changes in XPS spectra for all elements except for oxygen (Supplementary Figs. 10, 11). For stainless steel, the ratio of oxygen defects to M-O increased after one cycle of GSNO incubation, similar to before the calcination process (Fig. 3di), suggesting a decrease in the oxide layer. This implies the oxide layer had a significant effect on the catalytic performance of the calcinated wire given the decrease in NO generation after one GSNO cycle. On the other hand, this was not the case with stellite, where a low ratio of oxygen defects to M-O was still observed, similar to after the calcination

process (Fig. 4dii). However, additional C=O and C-O peaks were observed upon GSNO incubation.

Material integrity and performance evaluation

Thus far, we have successfully demonstrated that our heat treatment process enables the catalytic generation of NO from stainless steel and stellite wires. We investigated various parameters affecting NO generation, including wire length, kinetic generation rate, GSNO concentration, alternative NO prodrugs, and wire recyclability. However, recognizing that the heat treatment process could potentially alter mechanical properties, it is essential to evaluate these differences, as any changes could compromise the structural integrity of implants and increase the risk of failure. This section aims to highlight the differences in mechanical properties, rather than assert that the treated materials can still be used as implant materials. Further testing is required to ensure that they meet the necessary standards for medical implants, depending on their final application. To this end, tensile testing was carried out on both non-calcinated and calcinated stainless steel and stellite wires. The untreated and treated metal wires were subjected to

Fig. 8 | Effect of calcination temperature on NO release from stainless steel and stellite wires. i) Cumulative NO generation and ii) corresponding Raman spectra after incubating 5 non-calcinated or calcinated **a** stainless steel and **b** stellite wires in 200 μL of 50 μM GSNO in PBS for 8 hours at 37 $^{\circ}\text{C}$. Wires were calcinated at 300, 600, or 900 $^{\circ}\text{C}$ for 0.5 h. * $p < 0.05$, ** $p < 0.01$, *** $p < 0.001$ (ANOVA followed by Tukey post-hoc test). The dashed line represents the average concentration of NO generated by non-calcinated wires. $n \geq 3$; error bars and grey shaded area represent standard deviation.



controlled loading conditions until failure, allowing for the measurement of tensile strength, ductility, and Young's modulus (Fig. 11). The mechanical properties of both stainless steel and stellite wires showed small changes after calcination (Supplementary Table 2). Specifically, for stainless steel it was observed that after the heat treatment process, the tensile strength decreased from 1336.8 to 1318.4 MPa, the ductility as measured by tensile strain at maximum force decreased from 6.3 to 3.9%, and the Young's modulus increased from 32.4 to 43.2 GPa. On the other hand, for stellite the tensile strength increased from 1934.3 to 2436.5 MPa, while the ductility decreased from 8.2 to 6.5%, and the Young's modulus increased from 33.1 to 48.7 GPa. These results confirm that the calcination process does not adversely affect the critical mechanical properties of the metal wires, in both cases leading to a small increase in stiffness and decrease in ductility.

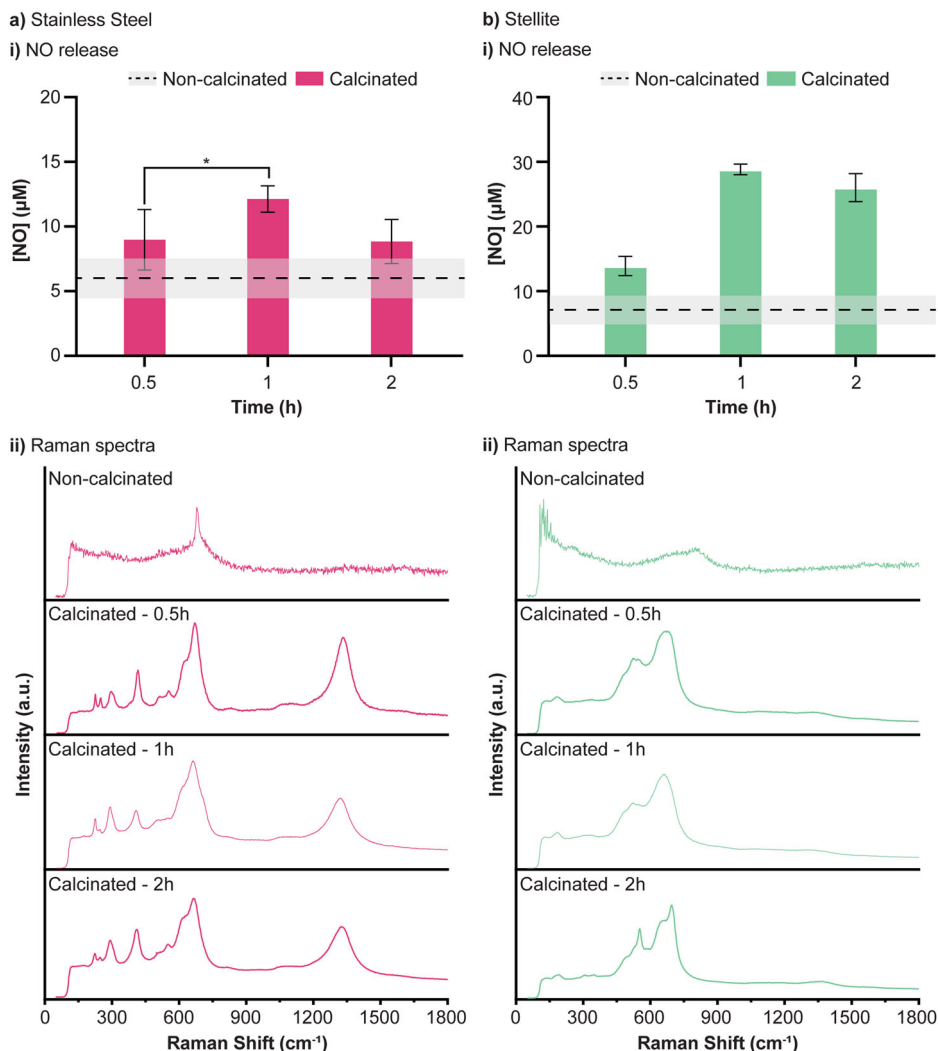
In addition to changes in mechanical properties, it is also important to evaluate leaching of metal ions into the surrounding environment. ICP-MS was used to quantify the elemental composition of the supernatant of solutions incubating untreated and treated wires at various time points (24 h, 1 week, 2 weeks, and 4 weeks). For both materials, an increase in elemental concentration was observed, suggesting the heat treatment process indeed enhances leaching of certain elements (Supplementary Tables 3, 4), albeit in the ppb range. It is therefore necessary to evaluate two additional variables: (i) the biological impact of increased ion release (reviewed in Section Cytotoxicity, rate of proliferation, and biofilm inhibition properties), as well as (ii) the effect these transition metal ions have on NO production. For the latter case, EDTA was added as a chelating agent to ensure NO generation in previous sections was not significantly affected by the metal ions

leached from the samples. Briefly, 5 non-calcinated or calcinated wires for both materials were incubated with GSNO in the presence of EDTA for 24 h and the NO generated was quantified (Supplementary Fig. 12). A small decrease in overall NO generation was observed for all cases, suggesting the leached metal ions did not significantly contribute to NO generation. It is important to acknowledge that implant materials must exhibit high corrosion resistance to withstand the harsh physiological environment within the human body. The calcination process, by altering the microstructure or surface characteristics of the alloy, may impact its corrosion resistance. While this study primarily focuses on the catalytic generation of NO, we recognize the importance of corrosion resistance in medical implants⁵⁸. Addressing the corrosion behavior of calcined alloys is outside the scope of this study. However, future investigations will be necessary to comprehensively assess their long-term stability in physiological conditions.

Cytotoxicity, rate of proliferation, and biofilm inhibition properties

Next, the biocompatibility of the heat-treated wires was evaluated in order to ensure the heat treatment process does not result in cell toxicity. Specifically, non-calcinated or calcinated wires were exposed to HUVEC or HCASMC for 24 h and an alamarBlue assay was used to confirm their viability after exposure. As shown in Fig. 12a, b, no decrease in cell viability was observed for either material regardless of being heat treated or not. Although the wires do not affect either cell viability, it is also important to determine whether they affect the rate at which the cells proliferate. To evaluate this, HUVEC or HCASMC were seeded with wires and their cell viability over a 3-day period was monitored. No

Fig. 9 | Effect of calcination time on NO release from stainless steel and stellite wires. i) Cumulative NO generation and ii) corresponding Raman spectra after incubating 5 non-calcinated or calcinated a stainless steel or b stellite wires in 200 μL of 50 μM GSNO in PBS for 8 hours at 37 $^{\circ}\text{C}$. Wires were calcinated at 600 $^{\circ}\text{C}$ for 0.5, 1, and 2 h. * $p < 0.05$, ** $p < 0.01$, *** $p < 0.001$ (ANOVA followed by Tukey post-hoc test). The dashed line represents the average concentration of NO generated by non-calcinated wires. $n \geq 3$; error bars and grey shaded area represent standard deviation.



difference in cell viability was observed for all materials, indicating the calcination process does not affect the rate at which cells proliferate (Fig. 12c, d). This was further supported by optical microscope images which showed the morphology and number of the cells did not change between samples for the same time points (Supplementary Figs. 13–16). Upon confirming the calcination process does not affect cell viability, the performance of the wires to inhibit biofilm formation was evaluated. As previously mentioned, biofilm formation in implantable medical devices

(e.g., stents, catheters, vascular grafts, etc.) are a key limitation towards their application⁵⁹, and NO has been reported to disperse biofilms by inducing bacterial death⁴⁸. Therefore, the gram-negative *Pseudomonas aeruginosa* (PAO1) was chosen to evaluate the antibiofilm properties of both wire materials. *Pseudomonas aeruginosa* was chosen as it is one of the most common pathogens causing nosocomial infections in hospitals⁶⁰. Briefly, bacterial suspensions of PAO1 were incubated with 5 stainless steel or stellite wires as well as GSNO (50 μM) and

Fig. 10 | Recyclability and long-term storage of non-calcinated and calcinated stainless steel and stellite wires. Cumulative NO generation after incubating 5 non-calcinated or calcinated a stainless steel or b stellite wires in 200 μL of 50 μM GSNO in PBS for 24 hours for 5 cycles at 37 $^{\circ}\text{C}$. c Cumulative NO generation after incubating 5 non-calcinated or calcinated 10-month stored stainless steel or stellite wires in 200 μL of 50 μM GSNO in PBS for 24 hours at 37 $^{\circ}\text{C}$. $n \geq 3$; error bars represent standard deviation.

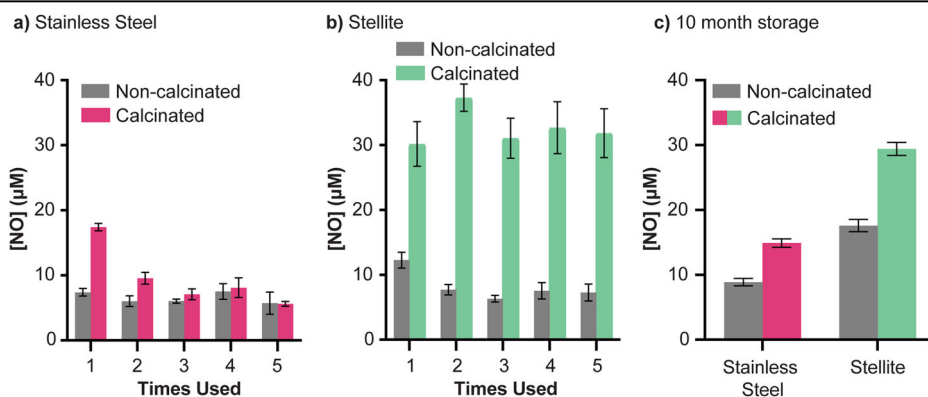
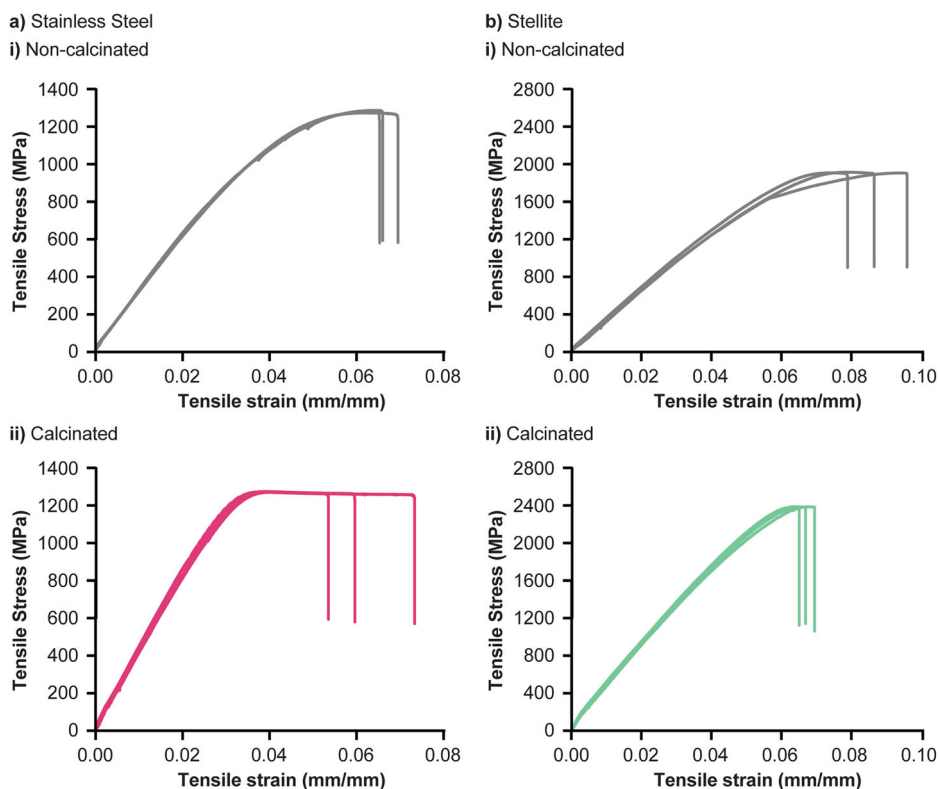


Fig. 11 | Tensile test of non-calcinated and calcinated stainless steel and stellite wires. **a** Tensile testing of i) non-calcinated and ii) calcinated stainless steel wires. **b** Tensile testing of i) non-calcinated and ii) calcinated stellite wires. Each test was conducted $n = 3$.



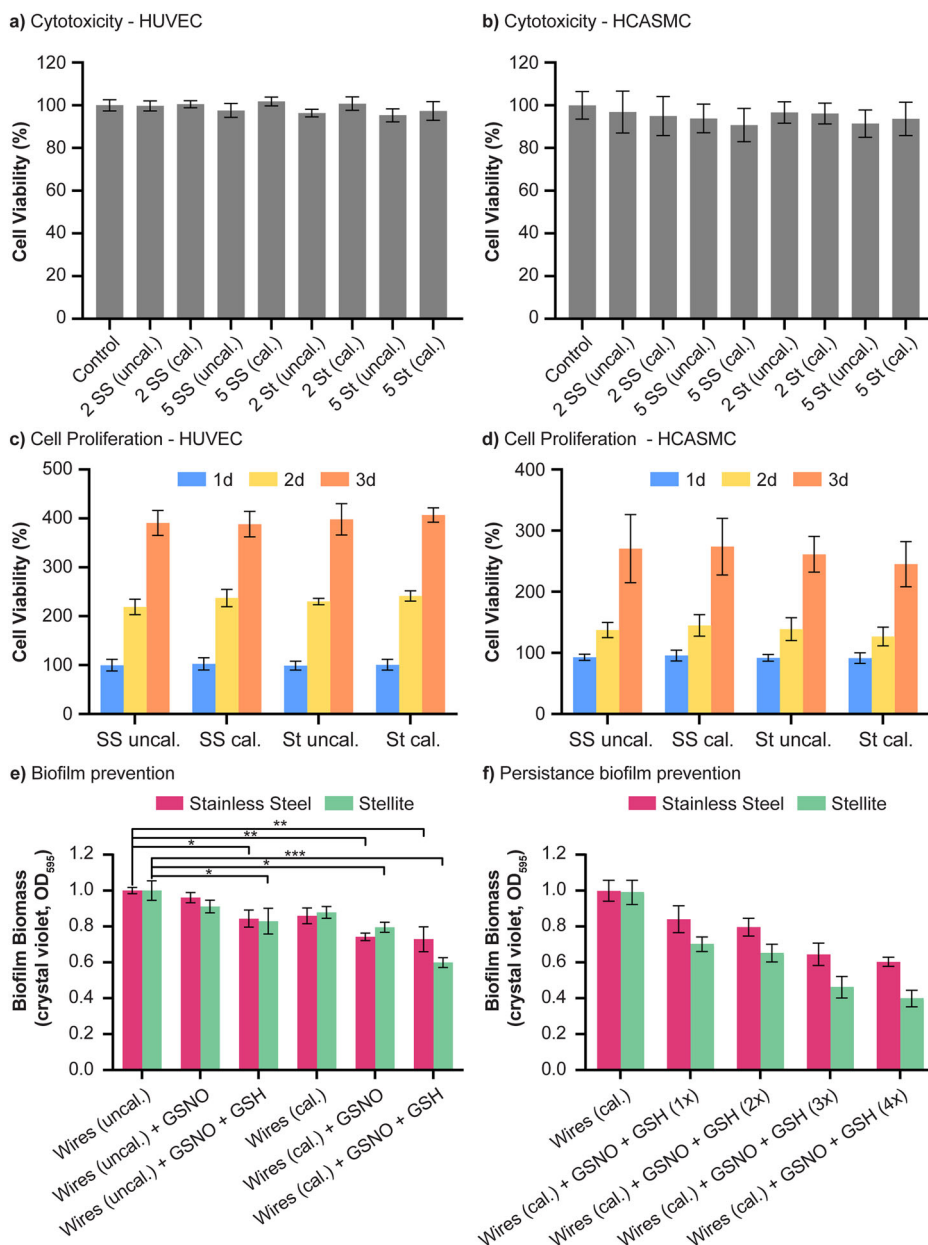
L-glutathione reduced (GSH) (1 mM) for 6 h. Then crystal violet staining was performed on the washed wires to quantify the biofilm (Fig. 12e). It should be noted that GSH was also included in this study as it is a biologically abundant biothiol⁶¹ and has been shown to act as a reducing agent⁶². Firstly, although the heat treatment process itself (wires non-cal. vs. wires cal.) resulted in an averaged 13% decrease in biofilm biomass prior to GSNO and GSH exposure, statistical analysis showed this difference was not significant. This was also the case between non-calcinated wires and non-calcinated wires exposed to GSNO. On the other hand, when exposed to GSNO and GSH, a statistically significant averaged decrease of 16% for both materials was observed. Consistent with previous results, calcinated stellite wires showed the highest reduction in biofilm formation when exposed to both GSNO and GSH, leading to 28% less biofilm formation compared to non-calcinated wires exposed to the same conditions, i.e. GSNO and GSH. When compared to non-calcinated wires which were not exposed to GSNO and GSH, a 40% inhibition in biofilm formation was observed. For stainless steel, the percentage decreases were 13 and 27%, respectively. These results demonstrate that the heat treatment process of the wires leads to an inhibition of bacterial biofilm formation via the generation of NO from GSNO. As demonstrated in the previous sections, the extent of biofilm inhibition can then be controlled by the amount of NO generated, which can be tuned by material choice, number of wires, GSNO concentration, and heat-treatment conditions. In practical applications, metallic implants will be subjected to a continuous exposure of GSNO and GSH rather than a single dose. Therefore, to assess the sustained antibiofilm efficacy under such conditions, repeated additions of GSNO and GSH were performed to simulate a biological environment. Specifically, GSNO and GSH were administered up to four times to determine if this would enhance the inhibitory effect. Consistent with expectations, both materials exhibited increased biofilm inhibition with additional GSNO and GSH doses (Fig. 12f). Comparatively, this approach aligns with recent studies on biofilm inhibition against *Pseudomonas aeruginosa* and other bacteria. Similar efficacy has been observed with other methods, including antibiotic-loaded block

copolymers (58% or 74%)⁶³, enzyme-loaded silver-doped silica nanoparticles (58.8% or 72.4%)⁶⁴, or hydrogels (82%-98% or 64%)⁶⁵, with inhibition ranges varying based on the bacterial species.

Conclusions

Metallic implants are valued for their exceptional biocompatibility and mechanical properties, however, implant-related infections remain a significant challenge in orthopaedic surgery. Various drug delivery methods, including surface-coated and drug-eluting implants, have shown effectiveness in mitigating this issue. However, these methods are limited by finite drug reserves and complex production processes. Likewise, techniques such as local drug synthesis, specifically enzyme-prodrug therapies, offer novel solutions yet are constrained by the inherent limitations of enzymes. Furthermore, these approaches would require a significant change in the implant's manufacturing process, leading to a need for reclassification and new approval from the FDA, compromising commercial feasibility⁶⁶. In response, we have explored a simpler alternative that can potentially maintain the device classification by harnessing the intrinsic qualities of the implant materials themselves for drug synthesis. Through a thermal treatment method, we have successfully imparted catalytic properties to commonly used implant materials, including stainless steel and stellite, specifically for the generation of NO. By modulating variables such as wire length, NO prodrug concentration, and heat treatment conditions, the NO generated could be controlled. Stellite proved to be a more ideal material which allowed for sustained NO delivery over multiple cycles without a loss in performance. We have also demonstrated the biocompatibility of the heat-treated wires, where both stainless steel and stellite wires exhibited no cytotoxic effects and did not disrupt cell proliferation rates, whilst displaying *Pseudomonas aeruginosa* biofilm inhibition properties. By relying on the intrinsic properties of the implant material itself to synthesize therapeutic agents, we have introduced a materials-driven solution that not only simplifies the process but also offers a promising avenue for the future of implant technology in healthcare. Moreover, this method offers a simple and efficient means of endowing potential

Fig. 12 | Cytotoxicity and biofilm inhibition properties of non-calcinated and calcinated stainless steel and stellite wires. Cytotoxicity of stainless steel or stellite wires before and after calcination towards **a** HUVEC and **b** HCASMC. Rate of proliferation of **c** HUVEC and **d** HCASMC in the presence of stainless steel or stellite wires before and after calcination. **e** Biofilm inhibition of non-calcinated and calcinated wires when exposed to 50 μ M GSNO and 1 mM GSH. **f** Biofilm inhibition of calcinated wires when exposed to 50 μ M GSNO and 1 mM GSH up to 4 times. * $p < 0.05$, ** $p < 0.01$, *** $p < 0.001$ (ANOVA followed by Tukey post-hoc test). $n \geq 3$; error bars represent standard deviation. SS stainless steel, St stellite, uncal. before calcination, cal. after calcination.



therapeutic properties to implant materials without the need for external chemicals or intricate enzymatic systems.

Methods

Materials

Stainless steel (AISI 316 L alloy, FeCr18Ni10Mo3, 250 μ m diameter), stellite (Co40Cr20Fe15Ni15Mo7Mn2CBe, 250 μ m diameter), titanium (250 μ m diameter), silver (250 μ m diameter), phosphate-buffered saline (PBS) tablets, ethylenediaminetetraacetic acid (EDTA), Griess reagent (modified), L-glutathione reduced (GSH), ethanol, ammonium chloride (NH₄Cl), potassium phosphate monobasic (KH₂PO₄), sodium chloride (NaCl), magnesium sulfate (MgSO₄), sodium phosphate dibasic (Na₂HPO₄), glucose, calcium chloride (CaCl₂), tryptone, and yeast were purchased from Merck (Australia). GSNO, DPTA NON-Oate, DETA NONOate, NOC-5, β -gal NONOate, and SNAP were purchased from Cayman Chemicals. Human umbilical vein endothelial cells (HUVECs) and MV Microvascular Endothelial Cell Growth Medium-2 BulletKit™ (EGM™-2) were purchased from Lonza Bioscience. Human coronary artery smooth muscle cells (HCASMC)

and smooth muscle cell growth medium kit were purchased from Cell Applications. AlamarBlue cell viability reagent was purchased from ThermoFisher Scientific. Ultrapure water (18.2 M Ω cm⁻¹) was provided by Arium pro Ultrapure Water Systems (Sartorius). PBS buffer was prepared by dissolving 1 PBS tablet in 200 mL ultrapure water and gently shaking until fully dissolved, for a final concentration of 10 mM phosphate buffer, 2.7 mM potassium chloride (KCl), and 137 mM sodium chloride (NaCl) (pH 7.4, 25 °C).

Wire calcination

Stainless steel, stellite, titanium, and silver wires 0.25 mm in diameter were cut to 5 mm in length using wire cutters and washed by sonicating (POWERSONIC 510) in acetone for 15 min followed by ultrapure water for 15 min. The wires were left to dry at room temperature and stored for later use. Washed wires are referred to as non-calcinated wires within this study. Unless otherwise stated, calcinated wires were prepared by heat-treating non-calcinated wires for 30 min at 600 °C (Nabertherm muffle furnace, P330, 30 - 3000 °C). A heating rate of 7.5 °C/min was used.

NO generation quantification via Griess Assay

NO generation was determined using a Griess Assay. This was done by mixing 90 μL of the sample supernatant with 90 μL of 40 mg mL^{-1} Griess reagent solution prepared in PBS, and allowed to react in a 96-well plate for 15 min. The absorption at 546 nm was then measured using a SpectraMax M5 microplate reader. The corresponding NO concentration was determined via a calibration curve.

Effect of wire length on NO generation

The effect of wire length on NO generation was determined by placing 0, 5, 10, 15, or 20 wires in a 1.5 mL glass vial, followed by the addition of 200 μL of 50 μM GSNO in PBS. The vial was immediately closed with a screw cap and placed inside an incubator at 200 RPM and 37 $^{\circ}\text{C}$ for 24 h, protected from light. NO generation was quantified via a Griess assay as previously outlined.

Kinetic NO generation

The NO generation over time was evaluated by placing 5 wires in a 1.5 mL glass vial, followed by the addition of 200 μL of 50 μM GSNO in PBS. The vial was immediately closed with a screw cap and placed inside an incubator at 200 RPM and 37 $^{\circ}\text{C}$ for 0.5, 1, 2, 4, 6, 8, or 24 h, protected from light. NO generation was quantified via a Griess assay as previously outlined.

Effect of GSNO concentration on NO generation

The tunability of NO generation was evaluated by placing 5 wires in a 1.5 mL glass vial, followed by the addition of 200 μL of 0, 12.5, 25, 50, 100, or 200 μM GSNO in PBS. The vial was immediately closed with a screw cap and placed inside an incubator at 200 RPM and 37 $^{\circ}\text{C}$ for 24 h, protected from light. NO generation was quantified via a Griess assay as previously outlined.

Alternative donors for NO generation

To determine whether the wires could also promote the generation of NO using other NO donors, 5 wires were placed in a 1.5 mL glass vial, followed by the addition of 200 μL of 50 μM DPTA NONOate, DETA NONOate, NOC-5, β -gal NONOate, or SNAP in PBS. The vial was immediately closed with a screw cap and placed inside an incubator at 200 RPM and 37 $^{\circ}\text{C}$ for 0.5 h, protected from light. NO generation was quantified via a Griess assay as previously outlined.

Effect of EDTA on NO generation

The effect of EDTA on NO generation was determined by placing 5 wires in a 1.5 mL glass vial, followed by the addition of 200 μL of 50 μM GSNO in PBS containing 0.1 mM EDTA. The vial was immediately closed with a screw cap and placed inside an incubator at 200 RPM and 37 $^{\circ}\text{C}$ for 24 h, protected from light. NO generation was quantified via a Griess assay as previously outlined.

Recyclability

The capacity for long-term NO generation was determined by placing 5 wires in a 1.5 mL glass vial, followed by the addition of 200 μL of 50 μM GSNO in PBS. The vial was immediately closed with a screw cap and placed inside an incubator at 200 RPM and 37 $^{\circ}\text{C}$ for 24 h, protected from light. NO generation was quantified via a Griess assay as previously outlined. The wires were then washed with ultrapure water via immersion and the above procedure was repeated a total of 5 times.

Cytotoxicity and rate of proliferation

HUVEC and HCASMC were cultured in EGMTM-2 BulletKitTM or smooth muscle cell growth medium kit, respectively, and subcultured when they reached a near confluent state. For the cytotoxicity test, HUVEC or HCASMC suspended in cell culture media were seeded onto 24-well plates with a density of 20000 cells/500 μL /well and incubated for 24 h at 37 $^{\circ}\text{C}$ in a 5% CO_2 humidified incubator. Then, the cell supernatant was aspirated and 500 μL of fresh media was added in addition to 2 or 5 non-calcinated or calcinated stainless steel or stellite wires, and incubated for another 24 h. Finally, the wires were gently removed, the supernatant was aspirated, the

cells were washed with sterile PBS, and fresh medium containing 10% alamarBlue was added to each well and incubated for 3 h, protected from light. The fluorescence values (Ex/Em = 560/590 nm) were measured using a microplate reader (SpectraMax M5) and the cell viability was calculated as cell viability (%) = $I_s/I_c \times 100\%$, where I_s represents the fluorescence of the experimental groups and I_c represents the fluorescence of control groups.

For the rate of proliferation test, HUVEC or HCASMC suspended in cell culture media were seeded onto 24-well plates with a density of 5000 cells/500 μL /well in addition to 5 non-calcinated or calcinated stainless steel or stellite wires. After a 24-, 48-, or 72-h incubation at 37 $^{\circ}\text{C}$ in a 5% CO_2 humidified incubator, the wires were gently removed, the supernatant was aspirated, the cells were washed with sterile PBS, and fresh medium containing 10% alamarBlue was added to each well and incubated for 3 h, protected from the light. The fluorescence values (Ex/Em=560/590 nm) were measured using a microplate reader (SpectraMax M5) and the cell viability was calculated as before.

Biofilm prevention

The laboratory strain *P. aeruginosa* (PAO1) was used to grow a biofilm. In all assays, a single colony of PAO1 was inoculated overnight in 10 mL of Luria Bertani medium (LB 10) at 37 $^{\circ}\text{C}$ with shaking at 180 RPM. LB 10 was prepared by mixing 10 g of tryptone, 5 g yeast extract, and 5 g NaCl in 1 L of ultrapure water followed by autoclaving at 120 $^{\circ}\text{C}$ for 25 mins. The overnight culture was diluted 1:200 in freshly prepared M9 minimal medium containing 48 mM Na_2HPO_4 , 22 mM KH_2PO_4 , 9 mM NaCl, and 19 mM NH_4Cl , pH 7.0, supplemented with 2 mM MgSO_4 , 100 μM CaCl_2 , and 20 mM glucose. The bacterial suspension was then aliquoted in a 24-well plate (Costar, Corning[®]) using 1 mL per well, each containing 5 wires. For GSNO treated samples, 20 μL of 2.5 mM GSNO prepared in M9 minimal medium was added to the respective wells. Where applicable, 20 μL of 50 mM GSH was also added into the sample wells. The plates were incubated at 37 $^{\circ}\text{C}$ with shaking at 180 RPM in an orbital shaker that does not stop agitation when the door is opened (model OM11, Ritek, Australia) and the biofilm cultures were allowed to grow for 6 h without any disruption. Biofilm biomass was quantified using the crystal violet (CV) staining method. Then, the culture supernatant was removed, and the well was washed once with 1 mL of PBS. The wires were then moved into a clean well before the addition of 1 mL 0.03% CV stain made from a 1:10 dilution of Gram crystal violet (BD) in PBS. The plates were incubated on the bench for 20 min before the wells were washed twice with PBS. The CV-stained biofilms were mixed with 1 mL 100% ethanol and quantified by measuring the OD₅₉₅ of the homogenized suspension (200 μL of aliquot) using a microtiter plate reader (FLUOstar Omega, BMG Labtech). All assays included two replicates and were repeated in at least three independent experiments.

The capacity for persistent biofilm prevention was determined by the addition of 20 μL of 2.5 mM GSNO and 20 μL of 50 mM GSH to the calcinated stellite and stainless steel wires. This addition was repeated every 2 h. Both GSNO and GSH were initially added to all samples (labelled as 1x, 2x, 3x, 4x) except the control sample. Identical amounts of GSNO and GSH were added to the 2x, 3x, and 4x wells after 2 hours of incubation. Subsequently, GSNO and GSH were added again to the 3x and 4x wells after an additional 2 hours of incubation. Lastly, GSNO and GSH were added to the 4x wells and incubated for another 30 minutes. The biofilm cultures in all wells were incubated for a total of 6.5 hours. The biofilm biomass was quantified with the same procedures listed above.

Characterization

FE-SEM/EDS. The morphology and elemental composition of the wires before and after calcination were characterized via field emission scanning electron microscopy (FE-SEM, FEI Nova NanoSEM 230) and energy dispersive spectroscopy (EDS, Bruker SDD-EDS), respectively. An acceleration voltage of 5 and 15 kV and a spot size of 3 and 5 were used for FESEM and EDS, respectively. Due to the nature of the material, no carbon or platinum coating was added.

Raman Spectra. The Raman spectra were obtained at room temperature using a Renishaw inVia Qontor confocal Raman microscope with a diode-pumped solid-state 532 nm laser, 1800 grooves/mm grating, and 100x objective (NA 0.85). An exposure time of 1 s, laser powder of 50%, and 120 accumulations were used.

AFM. The AFM measurements were performed on the Bruker Dimension Icon SPM equipped with a Nanoscope V controller. Peak force tapping mode with the SCANASYST-AIR probe (from Bruker AFM probes) was used to measure all the samples. The scan size was set to 2 μm . The scan rate was set to 0.7 Hz, with a peak force of approximately 800 pN. The feedback gain was adjusted accordingly to optimize tracking of the specimen surface, without any significant feedback noise. The resolution of the image was set to 512 pixels per line. AFM images were analysed using Gwyddion software, version 2.59.

XPS. XPS was conducted in tapping mode using a ESCALAB 250Xi (Thermo Scientific) with binding energies calibrated to the C1s line at 284.8 eV.

Tensile testing. A 5500 Series (5565) electromechanical Universal Testing Machine (Instron) was used to carry out the tensile test. Wire grips were used to securely fasten 60 cm of untreated or treated wire. A gauge length of 70 mm was used, with a clear distance between grips of 15 mm. Wires were wound twice around the grips. A rate of 0.5 mm/min was used.

ICP-MS. The supernatant (1 mL) of 30 non-calcinated or calcinated stainless steel or stellite wires placed in 1.2 mL of PBS for 24 h, 1 week, 2 weeks, or 4 weeks was mixed with 0.15 mL HNO₃ (70%), 0.05 mL H₂O₂ (~30%), and 0.2 mL HCl (~36%). Element concentrations were measured using inductively coupled plasma mass spectrometry (ICP-MS, Perkin Elmer, Nexion 5000 multi quad). The instrument settings included: ICP RF power: 1200–1500 Watt, vacuum pressure: $<8 \times 10^{-6}$ torr, pulse stage voltage: 800–1500 volt, analog stage voltage: - (1700–2300) volt, plasma gas flow: 15–17 L/min, auxiliary gas flow: 1–2 L/min, nebulizer gas flow: 0.85–1.2 L/min, lense voltage: 4–12 volt, cell gas: He, NH₃, O₂, CH₄. The instrument was calibrated with a freshly prepared series of standards from a stock standard solution which included the required element (at least 4 points including blank) before starting analysis of a batch.

Statistical Analysis

All data are presented as mean \pm standard deviation, with ≥ 3 independent replicates. One-way ANOVA was conducted with Tukey post hoc analysis. Statistical difference is denoted when $p < 0.05$. * $p < 0.05$, ** $p < 0.01$, *** $p < 0.001$, and **** $p < 0.0001$.

Reporting summary

Further information on research design is available in the Nature Portfolio Reporting Summary linked to this article.

Data availability

The authors declare that the data supporting the findings of this study are available within the paper and its supplementary information file or from the corresponding author upon reasonable request.

Received: 5 February 2024; Accepted: 5 July 2024;

Published online: 17 July 2024

References

1. Insights, F. B. *Orthopedic Implants Market Size, Share & COVID-19 Impact Analysis, By Product (Joint Reconstruction (Knee, Hip, and Extremities), Spinal Implants (Spinal Fusion Devices and Spinal Non-fusion Devices), Trauma Implants, and Others), By End-user (Hospitals & Ambulatory Surgery Centers and Orthopedic Clinics & Others), and*

Regional Forecast, 2023-2030, <https://www.fortunebusinessinsights.com/industry-reports/orthopedic-implants-market-101659> (2023).

2. Kim, T., See, C. W., Li, X. & Zhu, D. Orthopedic implants and devices for bone fractures and defects: Past, present and perspective. *Eng. Regen.* **1**, 6–18 (2020).
3. Jiao, J., Zhang, S., Qu, X. & Yue, B. Recent advances in research on antibacterial metals and alloys as implant materials. *Front. Cell. Infect. Microbiol.* **11**, 693939 (2021).
4. Alshimaysawee, S., Fadhel Obaid, R., Al-Gazally, M. E., Alexis Ramirez-Coronel, A. & Bathaei, M. S. Recent advancements in metallic drug-eluting implants. *Pharmaceutics* **15**, 223 (2023).
5. Raghavendra, G. M., Varaprasad, K. & Jayaramudu, T. In *Nanotechnology Applications for Tissue Engineering* (eds Sabu Thomas, Yves Grohens, & Neethu Ninan) 21–44 (William Andrew Publishing, 2015).
6. Izakovicova, P., Borens, O. & Trampuz, A. Periprosthetic joint infection: current concepts and outlook. *EFORT Open Rev.* **4**, 482–494 (2019).
7. Kuehl, R. et al. Time-dependent differences in management and microbiology of orthopaedic internal fixation-associated infections: an observational prospective study with 229 patients. *Clin. Microbiol. Infect.* **25**, 76–81 (2019).
8. Mortazavi, J. S. M., Schwartzberger, J., Austin, M. S., Purtill, J. J. & Parvizi, J. Revision total knee arthroplasty infection: incidence and predictors. *Clin. Orthop. Relat. Res.* **468**, 2052–2059 (2010).
9. Kapadia, B. H. et al. Periprosthetic joint infection. *Lancet* **387**, 386–394 (2016).
10. Margaryan, D. et al. Spinal implant-associated infections: a prospective multicentre cohort study. *Int. J. Antimicrob. Agents* **56**, 106116 (2020).
11. Lyndon, J. A., Boyd, B. J. & Birbilis, N. Metallic implant drug/device combinations for controlled drug release in orthopaedic applications. *J. Control. Release* **179**, 63–75 (2014).
12. Flemming, H.-C. et al. Biofilms: an emergent form of bacterial life. *Nat. Rev. Microbiol.* **14**, 563–575 (2016).
13. Koo, H., Allan, R. N., Howlin, R. P., Stoodley, P. & Hall-Stoodley, L. Targeting microbial biofilms: current and prospective therapeutic strategies. *Nat. Rev. Microbiol.* **15**, 740–755 (2017).
14. Bordbar-Khiabani, A., Yarmand, B., Sharifi-Asl, S. & Mozafari, M. Improved corrosion performance of biodegradable magnesium in simulated inflammatory condition via drug-loaded plasma electrolytic oxidation coatings. *Mater. Chem. Phys.* **239**, 122003 (2020).
15. Gimeno, M. et al. A controlled antibiotic release system to prevent orthopedic-implant associated infections: An in vitro study. *Eur. J. Pharm. Biopharm.* **96**, 264–271 (2015).
16. Wang, T. et al. Engineering immunomodulatory and osteoinductive implant surfaces via mussel adhesion-mediated ion coordination and molecular clicking. *Nat. Commun.* **13**, 160 (2022).
17. Meng, F., Yin, Z., Ren, X., Geng, Z. & Su, J. Construction of local drug delivery system on titanium-based implants to improve osseointegration. *Pharmaceutics* **14**, 1069 (2022).
18. Fejerskov, B., Jensen, N. B. S., Teo, B. M., Städler, B. & Zelikin, A. N. Biocatalytic polymer coatings: on-demand drug synthesis and localized therapeutic effect under dynamic cell culture conditions. *Small* **10**, 1314–1324 (2014).
19. Winther, A. K. et al. Enzyme prodrug therapy achieves site-specific, personalized physiological responses to the locally produced nitric oxide. *ACS Appl. Mater. Interfaces* **10**, 10741–10751 (2018).
20. Walther, R., Nielsen, S. M., Christiansen, R., Meyer, R. L. & Zelikin, A. N. Combatting implant-associated biofilms through localized drug synthesis. *J. Control. Rel.* **287**, 94–102 (2018).
21. Wang, F., Yang, J., Li, Y., Zhuang, Q. & Gu, J. Efficient enzyme-activated therapy based on the different locations of protein and prodrug in nanoMOFs. *J. Mater. Chem. B* **8**, 6139–6147 (2020).

22. Martijn, R., Jan, N. M. C. & Nico, P. E. V. Enzyme-catalyzed activation of anticancer prodrugs. *Pharmacol. Rev.* **56**, 53–102 (2004).
23. ter Meer, M. et al. Innate glycosidic activity in metallic implants for localized synthesis of antibacterial drugs. *Chem. Commun.* **55**, 443–446 (2019).
24. Schairer, D. O., Chouake, J. S., Nosanchuk, J. D. & Friedman, A. J. The potential of nitric oxide releasing therapies as antimicrobial agents. *Virulence* **3**, 271–279 (2012).
25. Lutzke, A., Melvin, A. C., Neufeld, M. J., Allison, C. L. & Reynolds, M. M. Nitric oxide generation from S-nitrosoglutathione: New activity of indium and a survey of metal ion effects. *Nitric Oxide* **84**, 16–21 (2019).
26. McCarthy, C. W., Guillory, R. J. II, Goldman, J. & Frost, M. C. Transition-metal-mediated release of Nitric Oxide (NO) from S-Nitroso-N-acetyl-d-penicillamine (SNAP): Potential applications for endogenous release of NO at the surface of stents via corrosion products. *ACS Appl. Mater. Interfaces* **8**, 10128–10135 (2016).
27. Tuttle, R. R., Rubin, H. N., Rithner, C. D., Finke, R. G. & Reynolds, M. M. Copper ion vs copper metal–organic framework catalyzed NO release from bioavailable S-Nitrosoglutathione en route to biomedical applications: Direct ¹H NMR monitoring in water allowing identification of the distinct, true reaction stoichiometries and thiol dependencies. *J. Inorg. Biochem.* **199**, 110760 (2019).
28. Ming, H. et al. A Mini Review of S-Nitrosoglutathione loaded nano/micro-formulation strategies. *Nanomaterials* **13**, 224 (2023).
29. Yang, T., Zelikin, A. N. & Chandrawati, R. Enzyme Mimics for the catalytic generation of nitric oxide from endogenous prodrugs. *Small* **16**, 1907635 (2020).
30. Wang, M.-M. et al. Multimetallic CuCoNi oxide nanowires in situ grown on a nickel foam substrate catalyze persulfate activation via mediating electron transfer. *Environ. Sci. Technol.* **56**, 12613–12624 (2022).
31. Zhou, X., Jing, G., Lv, B., Zhou, Z. & Zhu, R. Highly efficient removal of chromium(VI) by Fe/Ni bimetallic nanoparticles in an ultrasound-assisted system. *Chemosphere* **160**, 332–341 (2016).
32. Wang, W., Zhao, S., Tang, X., Chen, C. & Yi, H. Stainless steel catalyst for air pollution control: structure, properties, and activity. *Environ. Sci. Pollut. Res.* **29**, 55367–55399 (2022).
33. Godoy, M. L. et al. Stacked wire mesh monoliths for the simultaneous abatement of VOCs and diesel soot. *Catalysts* **8**, 16 (2018).
34. Chang, T., Zhang, L., Ma, R. & Liu, X. Thin-sheet monolithic-structured Pd–Au–CuOx/M-fiber (M = Ni, Al, SS, Cu) catalysts for gas-phase hydrogenation of dimethyl oxalate to ethylene glycol. *AIP Adv.* **11**, 075301 (2021).
35. Huang, Y. et al. Selective Se doping of NiFe₂O₄ on an active NiOOH scaffold for efficient and robust water oxidation. *Chin. J. Catal.* **42**, 1395–1403 (2021).
36. Liu, Y. et al. Development of MoS₂-stainless steel catalyst by 3D printing for efficient destruction of organics via peroxymonosulfate activation. *J. Environ. Sci.* **135**, 108–117 (2024).
37. Yao, Y. et al. Phase change on stainless-steel mesh for promoting sulfate radical formation via peroxymonosulfate oxidation. *Appl. Catal. B: Environ.* **278**, 119333 (2020).
38. Zhuo, C., Wang, X., Nowak, W. & Levendis, Y. A. Oxidative heat treatment of 316L stainless steel for effective catalytic growth of carbon nanotubes. *Appl. Surf. Sci.* **313**, 227–236 (2014).
39. Cao, D. et al. Volcano-type relationship between oxidation states and catalytic activity of single-atom catalysts towards hydrogen evolution. *Nat. Commun.* **13**, 5843 (2022).
40. Wang, W., Zhao, S., Tang, X., Chen, C. & Yi, H. Stainless steel catalyst for air pollution control: structure, properties, and activity. *Environ. Sci. Pollut. Res. Int* **29**, 55367–55399 (2022).
41. Ageev, E. I. et al. Influence of light incident angle on reflectance spectra of metals processed by color laser marking technology. *Opt. Quantum Electron.* **49**, 50 (2017).
42. Motallebzadeh, A., Dilawary, S. A. A., Atar, E. & Cimenoglu, H. High-temperature oxidation of stellite 12 Hardfacings: Effect of Mo on characteristics of oxide scale. *J. Mater. Eng. Perform.* **28**, 463–474 (2019).
43. Banús, E. D., Milt, V. G., Miró, E. E. & Ulla, M. A. Co,Ba,K/ZrO₂ coated onto metallic foam (AISI 314) as a structured catalyst for soot combustion: Coating preparation and characterization. *Appl. Catal. A: Gen.* **379**, 95–104 (2010).
44. Bortolozzi, J. P., Banús, E. D., Milt, V. G., Gutierrez, L. B. & Ulla, M. A. The significance of passivation treatments on AISI 314 foam pieces to be used as substrates for catalytic applications. *Appl. Surf. Sci.* **257**, 495–502 (2010).
45. Chen, L. et al. Effect of calcination temperature on structural properties and catalytic soot combustion activity of MnOx/wire-mesh monoliths. *Appl. Surf. Sci.* **467–468**, 1088–1103 (2019).
46. Born, R. et al. Surface analysis of titanium based biomaterials. *Fresenius' J. Anal. Chem.* **361**, 697–700 (1998).
47. Mazur, F., Lisi, F., Ma, Z. & Chandrawati, R. Wearable platform for low-dose inhaled nitric oxide therapy. *Adv. Mater. Technol.* **8**, 2201916 (2023).
48. Luo, Z., Ng, G., Zhou, Y., Boyer, C. & Chandrawati, R. Polymeric amines induce nitric oxide release from S-Nitrosothiols. *Small* **19**, 2200502 (2023).
49. Luo, Z. et al. Ceria nanoparticles as an unexpected catalyst to generate nitric oxide from S-Nitrosoglutathione. *Small* **18**, 2105762 (2022).
50. Yang, T., Fruergaard, A. S., Winther, A. K., Zelikin, A. N. & Chandrawati, R. Zinc oxide particles catalytically generate nitric oxide from endogenous and exogenous prodrugs. *Small* **16**, 1906744 (2020).
51. Zhou, Y. et al. Copper-doped metal–organic frameworks for the controlled generation of nitric oxide from endogenous S-nitrosothiols. *J. Mater. Chem. B* **9**, 1059–1068 (2021).
52. Broniowska, K. A., Diers, A. R. & Hogg, N. S-Nitrosoglutathione. *Biochim. et. Biophys. Acta (BBA) - Gen. Subj.* **1830**, 3173–3181 (2013).
53. Yang, Y., Huang, Z. & Li, L.-L. Advanced nitric oxide donors: chemical structure of NO drugs, NO nanomedicines and biomedical applications. *Nanoscale* **13**, 444–459 (2021).
54. Wu, X., Tang, X., Xian, M. & Wang, P. G. Glycosylated diazeniumdiolates: a novel class of enzyme-activated nitric oxide donors. *Tetrahedron Lett.* **42**, 3779–3782 (2001).
55. Melvin, A. C., Jones, W. M., Lutzke, A., Allison, C. L. & Reynolds, M. M. S-Nitrosoglutathione exhibits greater stability than S-nitroso-N-acetylpenicillamine under common laboratory conditions: A comparative stability study. *Nitric Oxide* **92**, 18–25 (2019).
56. Durán, F. G., Barbero, B. P. & Cadús, L. E. Preparation of MnOx/AISI 304 austenitic stainless steel monoliths for catalytic combustion of ethyl acetate. *Catal. Lett.* **141**, 1786–1795 (2011).
57. McGrady, J. et al. Investigation into the effect of water chemistry on corrosion product formation in areas of accelerated flow. *J. Nucl. Mater.* **493**, 271–279 (2017).
58. Shen, X. et al. Bone regeneration and antibacterial properties of calcium-phosphorus coatings induced by gentamicin-loaded polydopamine on magnesium alloys. *Biomed. Technol.* **5**, 87–101 (2024).
59. del Pozo, J. L. & Patel, R. The challenge of treating biofilm-associated bacterial infections. *Clin. Pharmacol. Ther.* **82**, 204–209 (2007).
60. Hou, M. et al. Deep profiling of the proteome dynamics of *Pseudomonas aeruginosa* reference strain PAO1 under different growth conditions. *J. Proteome Res.* **22**, 1747–1761 (2023).
61. Zhou, Y., Mazur, F., Fan, Q. & Chandrawati, R. Synthetic nanoprobe for biological hydrogen sulfide detection and imaging. *VIEW* **3**, 20210008 (2022).
62. Singh, S. P., Wishnok, J. S., Keshive, M., Deen, W. M. & Tannenbaum, S. R. The chemistry of the S-nitrosoglutathione/glutathione system. *Proc. Natl Acad. Sci. USA* **93**, 14428–14433 (1996).

63. Dai, X. et al. Protonation–activity relationship of bioinspired ionizable glycomimetics for the growth inhibition of bacteria. *ACS Appl. Biol. Mater.* **3**, 3868–3879 (2020).
64. Tasia, W. et al. Enhanced eradication of bacterial biofilms with DNase I-loaded silver-doped mesoporous silica nanoparticles. *Nanoscale* **12**, 2328–2332 (2020).
65. Hemmingsen, L. M. et al. Liposomes-in-chitosan hydrogel boosts potential of chlorhexidine in biofilm eradication in vitro. *Carbohydr. Polym.* **262**, 117939 (2021).
66. Xi, W. et al. Point-of-care antimicrobial coating protects orthopaedic implants from bacterial challenge. *Nat. Commun.* **12**, 5473 (2021).

Acknowledgements

R.C. acknowledges support from the National Health and Medical Research Council Emerging Leadership Investigator Grant (NHMRC APP1173428) and the UNSW Scientia Fellowship. C.B. acknowledges support from the Australian Research Council Laureate Fellowship (ARC FL220100016). This research used the facilities at the Mark Wainwright Analytical Centre Electron Microscope Unit at UNSW.

Author contributions

F.M. managed the project, designed research, developed methodologies, performed experiments, analyzed the data, and wrote and revised the paper. Y.Z. designed research and performed experiments. G.N. designed and performed biofilm inhibition experiments and analyzed the results. Q.F. analyzed XPS results. A.P. performed EDS imaging. C.B. designed and supervised the biofilm inhibition experiments and analyzed the results. R.C. conceived the idea, designed the research, revised the paper, and supervised the project. The manuscript was revised through the contributions of all authors.

Competing interests

Rona Chandrawati is an Editorial Board Member for *Communications Materials* and was not involved in the editorial review or the decision to publish this Article. All other authors declare no competing interests.

Additional information

Supplementary information The online version contains supplementary material available at <https://doi.org/10.1038/s43246-024-00564-7>.

Correspondence and requests for materials should be addressed to Rona Chandrawati.

Peer review information *Communications Materials* thanks Renchuan You and the other, anonymous, reviewer(s) for their contribution to the peer review of this work. Primary Handling Editors: Jet-Sing Lee. A peer review file is available.

Reprints and permissions information is available at <http://www.nature.com/reprints>

Publisher's note Springer Nature remains neutral with regard to jurisdictional claims in published maps and institutional affiliations.

Open Access This article is licensed under a Creative Commons Attribution 4.0 International License, which permits use, sharing, adaptation, distribution and reproduction in any medium or format, as long as you give appropriate credit to the original author(s) and the source, provide a link to the Creative Commons licence, and indicate if changes were made. The images or other third party material in this article are included in the article's Creative Commons licence, unless indicated otherwise in a credit line to the material. If material is not included in the article's Creative Commons licence and your intended use is not permitted by statutory regulation or exceeds the permitted use, you will need to obtain permission directly from the copyright holder. To view a copy of this licence, visit <http://creativecommons.org/licenses/by/4.0/>.

© The Author(s) 2024